Cracks as Efficient Tools to Mitigate Flooding in Gas Diffusion Electrodes Used for the Electrochemical Reduction of Carbon Dioxide

Ying Kong, Menglong Liu, Huifang Hu, Yuhui Hou, Soma Vesztergom, María de Jesus Gálvez-Vázquez, Iván Zelocualtecatl Montiel, Viliam Kolivoška,* and Peter Broekmann*

The advantage of employing gas diffusion electrodes (GDEs) in carbon dioxide reduction electrolyzers is that they allow CO_2 to reach the catalyst in gaseous state, enabling current densities that are orders of magnitude larger than what is achievable in standard H-type cells. The gain in the reaction rate comes, however, at the cost of stability issues related to flooding that occurs when excess electrolyte permeates the micropores of the GDE, effectively blocking the access of CO_2 to the catalyst. For electrolyzers operated with alkaline electrolytes, flooding leaves clear traces within the GDE in the form of precipitated potassium (hydrogen)carbonates. By analyzing the amount and distribution of precipitates, and by quantifying potassium salts transported through the GDE during operation (electrolyte perspiration), important information can be gained with regard to the extent and means of flooding. In this work, a novel combination of energy dispersive X-ray and inductively coupled plasma mass spectrometry based methods is employed to study flooding-related phenomena in GDEs differing in the abundance of cracks in the microporous layer. It is concluded that cracks play an important role in the electrolyte management of CO_2 electrolyzers, and that electrolyte perspiration through cracks is paramount in avoiding flooding-related performance drops.

1. Introduction

Rising levels of atmospheric CO_2 as a dominant greenhouse gas have motivated endeavors to curb carbon emissions and utilize excess CO_2 to produce valuable resources.[1] The electrochemical reduction of CO_2 (denoted hereafter ERCO$_2$) allows not only its conversion to fuels and feedstock chemicals of high added value, but also the simultaneous storage of electrical energy originating from intermittent renewable sources.[2]

ERCO$_2$ operating at commercially relevant reaction rates (current densities) requires efficient and stable catalysts and facile mass transport of reactants and products with minimized energy losses.[3] Gas diffusion electrodes (GDEs) circumvent the problem of limited solubility and slow diffusion of CO_2 in aqueous media by delivering this reactant to the catalyst layer via gas phase.[3–6]

In GDEs, the catalyst layer is located on a supportive gas diffusion layer (GDL) that is composed of a carbon fiber layer (CFL) and a microporous layer (MPL),[4] as shown in **Figure 1**. Besides the reactant delivery, the GDL enables the release of gaseous reaction products, serves as a mechanical support and electrical contact for the catalyst, and plays important role in controlling the amount of electrolyte in the catalyst layer.[4,7,8] GDEs operating in alkaline aqueous electrolytes show highly active and selective ERCO$_2$ toward target products (like CO) due to the combination of reduced ohmic drops,[3,9] favorable electrode kinetics,[3,10–14] and suppression of the electrochemical reduction of water (ERH$_2$O) as a parasitic reaction.[15]

Y. Kong, M. Liu, H. Hu, Y. Hou, S. Vesztergom, M. de J. Gálvez-Vázquez, I. Zelocualtecatl Montiel, P. Broekmann
Department of Chemistry, Biochemistry and Pharmaceutical Sciences
University of Bern
3012 Bern, Switzerland
E-mail: peter.broekmann@unibe.ch

The ORCID identification number(s) for the author(s) of this article can be found under https://doi.org/10.1002/smtd.202200369.

Y. Kong, M. Liu, Y. Hou, P. Broekmann
National Centre of Competence in Research (NCCR) Catalysis
University of Bern
3012 Bern, Switzerland

S. Vesztergom
Department of Physical Chemistry
Eötvös Loránd University
1117 Budapest, Hungary

V. Kolivoška
J. Heyrovský Institute of Physical Chemistry of the Czech Academy of Sciences
18223 Prague, Czech Republic
E-mail: viliam.kolivoska@jh-inst.cas.cz

**ADVANCED
SCIENCE NEWS**

www.advancedsciencenews.com
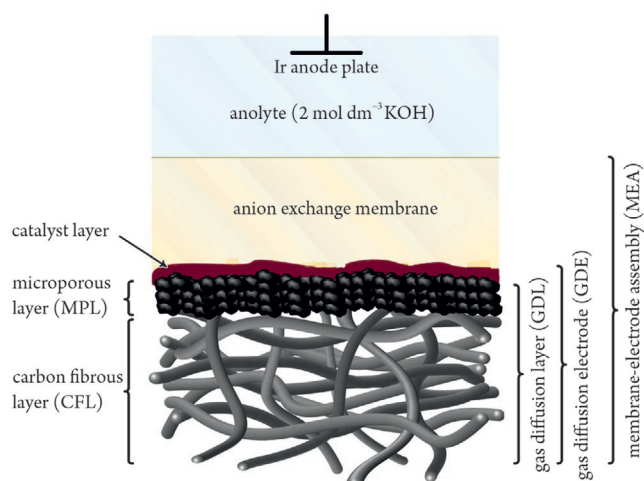
**small
methods**

www.small-methods.com

Figure 1. Schematic depiction of the zero-gap gas diffusion electrode (ZG GDE).

GDEs interfaced to ion exchange membranes, as shown in Figure 1, constitute membrane-electrode assemblies (MEAs),[16] allowing for decreased ohmic losses,[17] improved catalyst stability, and avoidance of problems due to the formation of gaseous products directly at electrode/electrolyte interfaces.[18]

Reactor arrangements based on MEAs were originally developed in the field of proton exchange membrane fuel cells (PEMFCs).[19] In PEMFCs, both the cathode and the anode are of a GDE structure, and are separated by a thin membrane. ERCO$_2$ electrolyzers often involve a configuration (see Figure 1 for a scheme; Figure S1, Supporting Information for detailed assembly) in which only the cathode is of a MEA structure.[20–22] This configuration is denoted further as a zero-gap GDE (ZG GDE) because the GDE cathode is in a direct contact with the membrane that separates it from the electrolyte solution (the anolyte) that contains the anode.

Despite differences in their mode of operation (electrical-to-chemical vs chemical-to-electrical energy conversion) and in their underlying chemistry, ZG GDE ERCO$_2$ electrolyzers and PEMFCs share several important aspects considering their water (electrolyte) management. In PEMFCs, H$^+$ ions resulting from the anodic oxidation of hydrogen are transported through the membrane to the cathode, where they are combined with electrons and oxygen to form water as the reaction product. In ZG GDE ERCO$_2$ electrolyzers, the membrane has essentially two roles: it controls the amount of water (that acts as a reactant of ERCO$_2$, and the absence of which can cause kinetic limitations[6]) and ensures that gaseous products formed by ERCO$_2$ in the catalyst layer cannot enter the anode compartment.

Insufficient hydration of the membrane can cause, both in PEMFCs and ZG GDE ERCO$_2$ electrolyzers, an increased cell resistance and pronounced energy losses, while excess hydration can lead to the flooding of the GDL and hence compromised transport of gaseous reactants toward the catalyst.[4]

The flooding of GDLs should be understood as a complex phenomenon that depends on diverse physico-chemical processes. System properties influencing flooding include the wettability of GDEs[8,23–29] and its dependence on the applied electrode potential (electrowetting),[30–40] the pH of the electrolyte,[30] the humidity of the reactant gases,[41,42] the presence of reaction intermediates[30] and products,[43] the temperature[30]

and pressure[31,32,37,38] gradients across the cell, as well as the thickness of the employed membranes.[29]

In PEMFC research, the inspection of flooding phenomena has reached a significant degree of maturity.[19,44–47] The distribution of water in the interior of fuel cell structures has been visualized under operando conditions, for example, by optical microscopy (OM), magnetic resonance imaging, neutron imaging, environmental scanning electron microscopy (SEM), X-ray computed tomography, and fluorescence microscopy.[48–50]

Strategies to mitigate flooding in PEMFCs involve the use of MPLs with large voids[51,52] comprising both naturally formed structures (pores[53,54] and cracks[55–58]) and artificially designed architectures (holes[59] and grooves[60]). These bigger voids in the MPLs exhibit a smaller capillary pressure and hydrodynamic resistance compared to that of micropores. Thus, water formed in the cathode catalyst layer can preferentially be drained through the larger voids, reaching the CFL and finally escaping the fuel cell via flow channels and gas outlet. When large voids with appropriate abundance and distribution are present, micropores remain dry and keep their ability to function as efficient transport channels for gaseous reactants.

In the ERCO$_2$ field, flooding has been reported for GDEs either directly interfaced to liquid electrolytes[8,10,11,25,26,28,32–34,36–40,61–70] or blanketed by ion exchange membranes.[22,27,29,41,42,65,71–74] Flooding in ERCO$_2$ electrolyzers was often found to be accompanied by the appearance of precipitated salts inside or on the surface of GDEs.[9,11,22,28,33,34,36,38,39,41,42,61,64–66,68,69,74–76] These salts are either themselves constituents of the electrolyte solution or are formed when such a constituent reacts with CO$_2$. Both flooding and salt precipitation can hinder or even completely block the transport of CO$_2$ to the catalyst. As a result, a transition from ERCO$_2$ to ERH$_2$O is observed, leading to a significant drop of the overall Faradaic efficiency of ERCO$_2$.

In ERCO$_2$ electrolyzers employing alkaline electrolytes, the flooding of GDEs, and the appearance of precipitates within the GDE structure are mutually perpetuating processes. As some of the alkaline electrolyte appears in the GDE, it combines with the CO$_2$ supply gas to form potassium carbonate (or bicarbonate) precipitates. These salt formations decrease the hydrophobicity of the GDE, resulting in the permeation of even more electrolyte to the MPL and the formation of additional amounts of the precipitate.[68]

As a consequence, the appearance of carbonate precipitates within a GDE structure during electrolysis can be regarded as a tracer of flooding. In this vein, several authors have described flooding phenomena by visualizing potassium (as the electrolyte cation) on the surface[22,28,66] or within the interior[34,35,68,69,72,76] of GDEs, by the application of SEM complemented by energy dispersive X-ray (EDX) elemental mapping or by X-ray micro-computed tomography.[66,76] While these SEM-EDX works successfully showed that the appearance of potassium containing precipitates in GDE structures can be interpreted as a sign of flooding, they did not attempt to quantify the distribution of precipitates within the GDE, and to establish a correlation between the latter and the observed performance losses of the electrolyzer. The reason behind this is most likely that EDX is mostly considered a qualitative technique, yielding elemental maps that are not directly (that is, not quantitatively) comparable. This gap can however be bridged by the application of a novel method, based on the combination of cross-sectional EDX measurements

with an inductively coupled plasma mass spectrometry (ICP-MS) based determination of the total potassium content accumulated within a GDE structure upon the electrolysis.[77]

Note here that from the viewpoint of catalytic performance and stability, not only the total electrolyte content in a GDE but also its spatial distribution may become decisive. While the occurrence of potassium inside the micropores of the MPL can be interpreted as a sign of flooding with high certainty, its appearance in the CFL is not necessarily to be linked to flooding of micropores. In several works, the transport of the liquid electrolyte through the entire GDE (further referred to as electrolyte perspiration) was reported.[37–39,41,66,68,70] It is likely—especially based on what was said above about PEMFCs[51–60]—that the electrolyte perspiration through larger structures in the MPL involving cracks can prevent or at least delay the flooding of the micropores.

In the ERCO$_2$ field, recent works have demonstrated that cracks in the MPL facilitate the reaction due to augmented mass transport of gaseous CO$_2$ to the catalyst[78] and removal of excess electrolyte from the catalyst layer.[37] To the best of our knowledge, however, there is no systematic work studying the impact of MPL cracks on the catalytic activity and water management in ERCO$_2$ electrolyzers, as was carried out for PEMFCs.[55,57] While flooding of GDEs by liquid water formed as the reaction product represents the only barrier for the gas transport in PEMFCs, ERCO$_2$ is further complicated by the intrusion of the electrolyte ions into GDEs, potentially leading to salt precipitation. Exploring the electrolyte transport through MPLs with systematically varied architectures thus becomes the aim of this paper, with the ultimate goal of avoiding electrode flooding and salt precipitation in commercial ERCO$_2$ reactors.

Here we perform a series of galvanostatic experiments in a ZG GDE electrolyzer operated with alkaline anolyte. We employ different GDEs, the MPLs of which exhibit a varied abundance of cracks. To allow for a straightforward monitoring of reaction rates, we employ silver as the ERCO$_2$ catalyst, capable of producing CO with near-unity Faradaic efficiency.[8,10,12–14,16,21,22,27–29,36,38,39,41,42,66,68,70,71,75,76] The evolution of the catalytic performance is inspected by online gas chromatographic monitoring of CO and H$_2$, the latter being the product of ERH$_2$O and hence a fingerprint of electrolyte management deficiencies. Additionally, cell resistance and voltage and surface wettability of GDEs are monitored in the course of the electrolysis. We further utilize potassium as the cation of the employed electrolyte to visualize and quantify flooding and perspiration in the interior of GDEs, based on a recently developed, robust analytical approach that combines cross-sectional EDX elemental mapping and ICP-MS methods.[77] In addition, we monitor the perspiration rate by determining the amount of potassium in the perspirate, employing ICP-MS.

To the best of our knowledge, we perform and present here the first systematic study of flooding phenomena in GDEs at varied stages of the electrolysis, for GDEs with systematically varied microarchitecture. Our results shed light on an important, yet still unaddressed question of ERCO$_2$ engineering, namely, that submillimeter cracks in the MPL of GDEs applied for CO$_2$ electrolysis play a key role in the electrolyte management, and that by providing direct means for electrolyte drainage, cracks can efficiently prevent (or at least delay) the flooding of the catalyst layer.

2. Results and Discussion

The presented work aims at exploring the impact of the MPL structure with the emphasis on naturally occurring cracks on the catalytic activity and electrolyte management in ERCO$_2$ realized in an alkaline ZG GDE-based electrolyzer (full and cross-sectional drawings are shown in Figure S1, Supporting Information).[22,79]

We have selected four commercial GDLs as catalyst supports for our experiments, all of them having a bilayer structure composed of a CFL and an MPL. Three GDLs (36BB, 39BB, and 39BC) contain cracks in their MPLs. The fourth GDL (H23C8) has a crack-free MPL and is utilized as a reference system. For all four GDLs, the CFL is composed of coarse fibers. The surfaces of all GDLs were air-brushed with a catalyst ink containing silver nanowires (see the Experimental Section for details). The use of a catalyst ink based on nanowires was motivated by the assumption that assemblies of these quasi-1D objects form thin layers uniformly covering MPL surfaces and crack walls, without permeating into the interior of micropores.[70] For all four GDEs, the mass loading of silver was constant and equal to ≈40 µg cm^{-2}, as verified by ICP-MS analysis (see the Experimental Section for details). Representative top-down OM images of as-prepared GDEs are shown in **Figure 2**.

The optical micrographs of Figure 2 are very similar to those shown in Figure S2, Supporting Information, taken from bare GDL surfaces unmodified by catalyst ink deposition. This suggests that the air brush deposition leads to uniform catalyst layers without localized accumulation of deposits on the GDL surface or in cracks.

To inspect the structure of the formed catalyst layers in more detail, surfaces of as-prepared GDEs were further imaged by top-down SEM (also shown in Figure 2). For all four GDEs, Ag nanowires are well discerned, appearing as a collection of cylindrical objects with a diameter of ≈100 nm and a length of several micrometers, oriented parallel to the electrode surface. The small spherical features seen in the top-down SEM images of Figure 2 are attributed to the carbon black particles of the catalyst ink. High-resolution cross-sectional focused ion beam SEM images of top parts of MPLs (Figure S3, Supporting Information) demonstrate that the formed catalyst layers are 100 to 300 nm thick and involve one to three layers of Ag nanowires.

To investigate the permeation of the catalyst ink into the interior features of MPLs (micropores and cracks), cross sections of as-prepared GDEs were further inspected by SEM imaging combined with the EDX mapping of silver (Figure 2). For the non-cracked MPL (H23C8), the silver signal is confined to the top part of the MPL, confirming that Ag nanowires do not permeate micropores.

For cracked MPLs (36BB, 39BB, and 39BC) we first focused (in Figure 2) on regions containing cracks appearing as shaded features in the centers of cross-sectional SEM images. The corresponding EDX maps show a strong silver signal in the cracks, confirming that the catalyst ink permeates into the interior of the GDE through the cracks. For all three cracked MPLs, we performed the same analysis for regions with no cracks, with results shown in Figure S3, Supporting Information. In all cases, the silver signal is confined to the top of MPLs, similarly as for the non-cracked MPL (H23C8, Figure 2).
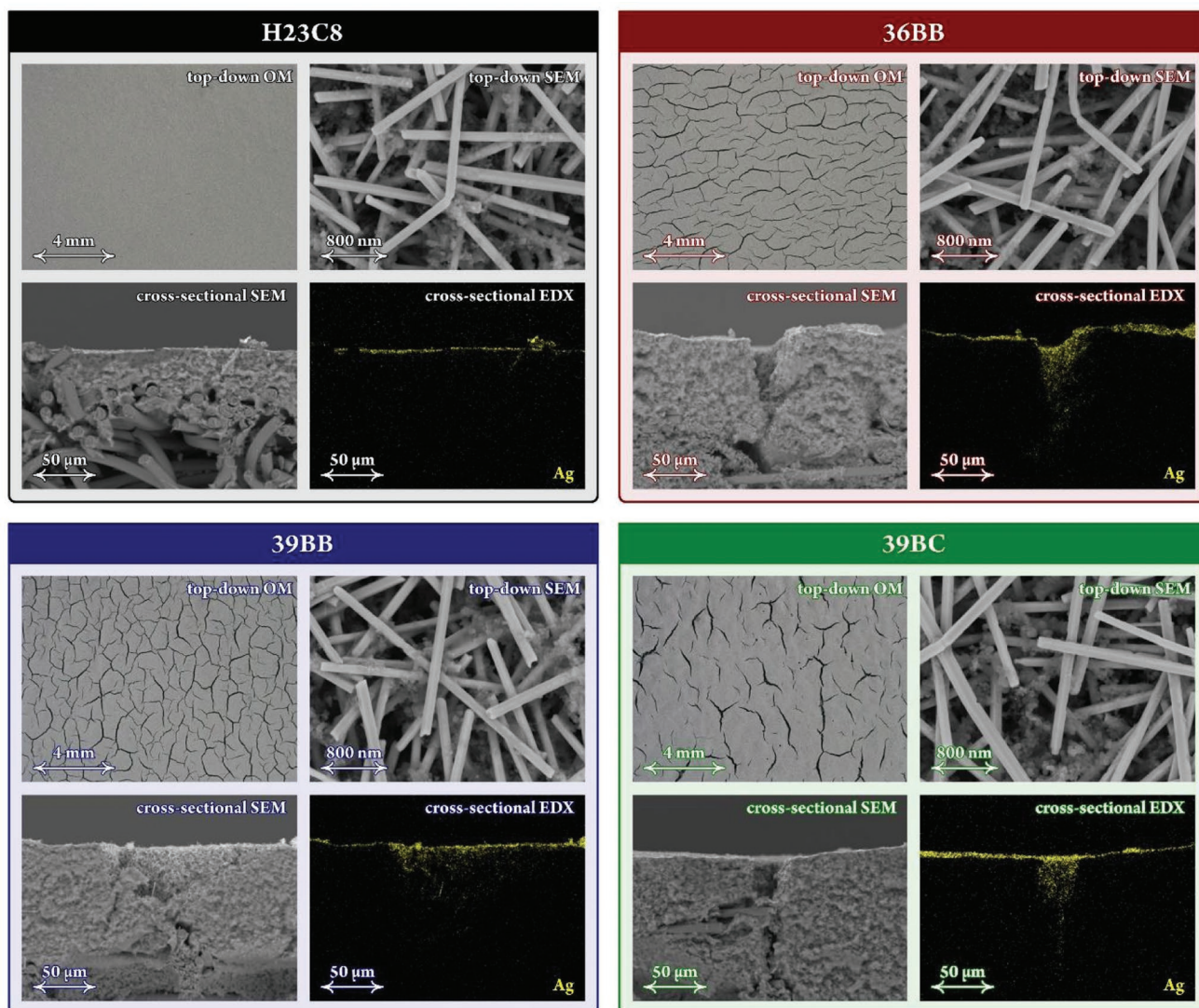
Figure 2. Representative top-down OM and SEM images, and cross-sectional SEM images and silver EDX maps of as-prepared GDEs.

One can conclude that the employed air brush deposition protocol leads to surfaces of MPLs completely covered by a thin catalyst layer that permeates into cracks, but leaves micropores unmodified. Such arrangement of the catalyst layer spatially decouples the target electrochemical process ($ERCO_2$) from the mass transport and charge transport phenomena occurring in the MPL, which is essential for the rigorous interpretation of relationships between the MPL structure, catalytic performance, and electrolyte management characteristics addressed in this work.

With regard to the distribution of cracks (see the optical micrographs of Figure 2 for catalyst ink-covered and Figure S2, Supporting Information for bare GDLs), it can be said that the H23C8 MPL has an almost featureless surface. Surfaces of the other three MPLs contain cracks that appear as distinct, elongated, and dark features. Cracks have no preferential orientation and enclose otherwise flat regions. White-light interferometry images of the pristine GDLs, as well as those of GDLs covered by a catalyst ink (taken before or following electrolysis, Figure S4, Supporting Information) exhibit the same crack distribution that seems undisturbed both by the catalyst ink coating and by subsequent electrolysis.

The pixel-by-pixel analysis of the top-down optical micrographs shown in Figure 2 allowed us to determine the relative occurrence of cracks on the MPL surface, denoted further as the surface crack ratio (CR). Obtained values are listed in **Table 1** and range from 0% to 21%. The characteristic width of cracks (≈100 µm for 36BB and 39BB, 100 to 200 µm for 39BC) is comparable to the thickness of the MPLs (also listed in Table 1), suggesting that most cracks span over the entire MPL depth.

Table 1 also lists void ratio values of entire GDLs, CFLs, and MPLs. These values were determined by densitometry, as described in the Experimental Section. The void ratio values of MPLs (further referred to as VR values) represent the cumulative porosity of MPLs; that is, the porosity that accounts for both cracks and micropores. The structure of micropores is partially resolved in SEM images presented in Figure S2, Supporting Information. As seen in Table 1, VR values scale with CR values, indicating that cracks are significant contributors to the overall porosity of MPLs. However, the differences

Table 1. Physical characteristics of GDLs used in this work. See the Statistical Analysis in the Experimental Section for more information on statistics.

	Entire GDL		CFL		MPL			
	Thickness [µm]	Void ratio [%]	Thickness [µm]	Void ratio [%]	Thickness [µm]	Void ratio (VR) [%]	Crack ratio (CR) [%]	Pores in solid (PS) [%]
H23C8	235 ± 3	60 ± 4	194 ± 5	67 ± 4	41 ± 2	30 ± 8	0 ± 0	30 ± 8
36BB	256 ± 9	70 ± 3	160 ± 20	73 ± 1	97 ± 11	68 ± 4	9 ± 2	64 ± 4
39BB	295 ± 15	81 ± 5	197 ± 22	82 ± 2	98 ± 7	78 ± 8	16 ± 4	74 ± 10
39BC	267 ± 7	72 ± 1	138 ± 21	66 ± 2	129 ± 14	78 ± 4	21 ± 4	72 ± 5

between VR values of cracked MPLs and the one obtained for the non-cracked MPL are more pronounced than the respective CR values, suggesting that cracked MPLs also exhibit a higher microporosity than crack-free MPLs. To quantify this observation, we introduce here a parameter termed the porosity of solid regions (PS) of MPLs, defined as

$$PS = \frac{VR - CR}{1 - CR} \quad (1)$$

Obtained PS values of all applied MPLs are also presented in Table 1. We presume that cracks formed in MPLs result from drying as a part of the manufacturing process of GDLs.[28] The comparison of PS and CR values suggests that the formation of cracks during the drying process is more likely for more porous MPLs. Results of combined OM and SEM imaging (Figure S2, Supporting Information) further show that the characteristic dimensions of cracks and micropores differ by at least two orders of magnitude. This difference has, as will be demonstrated, a huge impact on the capillary phenomena occurring in MPLs, being one of the key factors influencing the electrolyte management and hence catalytic performance of ZG GDEs.

For $ERCO_2$ testing, each GDE prepared and characterized as described above was blanketed by an anion exchange membrane and integrated in the electrolyzer, forming a ZG GDE (see Figure S1, Supporting Information for the arrangement of the electrolyzer and the Experimental Section for details). The electrolysis was performed and monitored under galvanostatic conditions with the GDE being continuously fed by a stream of humidified CO_2. **Figure 3** shows the evolution of the Faradaic efficiency (FE) values of CO obtained for all four ZG GDEs, expressed as a function of time as well as normalized charge passed in the electrolysis.

The charge normalization is based on the geometric area of the ZG GDE/anolyte interface, and the presented FE(CO) values were obtained by gas chromatography (GC) monitoring of the formed CO quantity during electrolysis (see the Experimental Section). For all ZG GDEs, CO is initially formed with near-unity FE, confirming that the catalyst shows high activity toward $ERCO_2$.

In the course of the electrolysis, significant differences in the evolution of FE(CO) values are noticed. For the crack-free MPL (H23C8), a fast decline in the CO production rate and a concomitant increase of the H_2 production rate are observed. The observed loss of CO production specificity may either be caused by a gradual degradation of the active catalyst sites, or by the retarded mass transport of CO_2 toward the catalyst layer.

For GDEs involving cracked MPLs, a markedly different evolution of FE(CO) values is observed. The GDE with the intermediate abundance of cracks (36BB, red) starts losing its catalytic

activity roughly upon one-third of the electrolysis time. GDEs with higher crack abundance (39BB and 39BC, blue and green) continue to generate CO with near-unity FE values till the very end of the electrolysis. To reveal the origin of differences in the catalytic behavior, we performed identical location SEM studies of the catalyst layers deposited on H23C8 and 39BC GDLs (systems showing the smallest and the largest drop in the catalytic activity) before and after the electrolysis. For both systems, the obtained micrographs (Figure S5, Supporting Information) demonstrate that the electrolysis causes no visible changes in the nanomorphology of the catalyst. To exclude the influence of the electron beam used in SEM on the catalytic behavior and subsequent imaging,[80] we have further inspected random
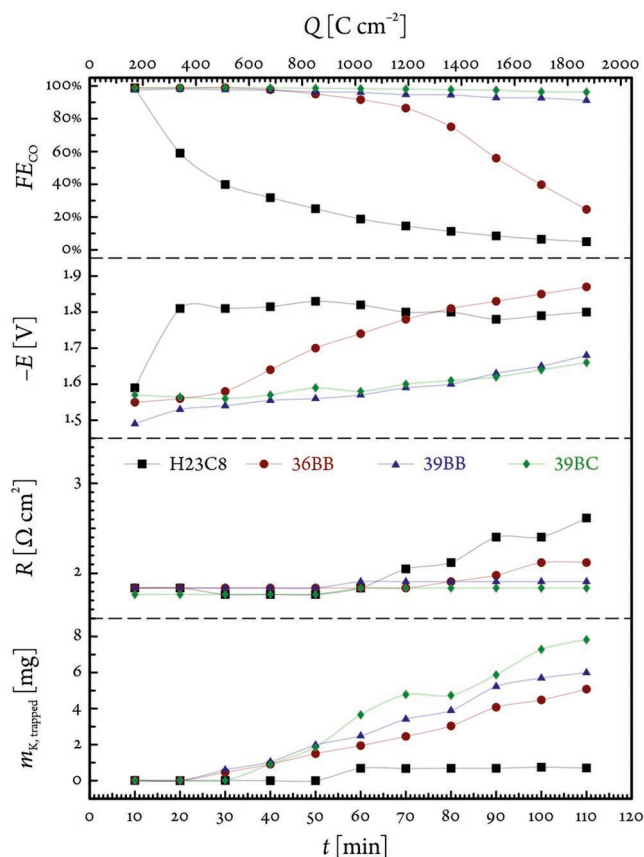

Figure 3. Faradaic efficiency of CO, ohmic drop-corrected cell voltage, normalized cell resistance, and the amount of potassium found by ICP-MS in the outlet trap plotted as a function of time and normalized charge passed in the electrolysis. Experiments were performed in the galvanostatic regime at −283 mA cm⁻², employing aqueous 2 M KOH as anolyte. A humidified CO_2 stream was fed to the GDE during the experiment at constant flow rate of 18 mL min⁻¹.

locations of the catalyst layer, not imaged prior to the electrolysis, again showing no signs of degradation (random location SEM micrographs are also shown in Figure S5, Supporting Information). Keeping in mind that catalyst loading and conditions applied in the electrolysis were identical for all four ZG GDEs, this suggests that a decline of the CO production rate observed for H23C8 and 36BB is not caused by the degradation of catalytic sites.

Employing a 36BB GDE selected for the demonstration, we further performed a follow-up electrolysis with a previously once-used electrode, preceded by a rinsing/drying step (see the Experimental Section for details). The catalytic activity of the electrode at the beginning of the follow-up electrolysis was largely restored (Figure S6, Supporting Information). This result not only confirms that the flooded electrolyte may be at least partially removed from the interior of the GDE, but additionally demonstrates that electrodes may be reused. The degradation of the catalyst was further excluded by identical and random location SEM studies performed before the initial and after the follow-up electrolysis (micrographs are also shown in Figure S6, Supporting Information).

The observed differences in the evolution of FE(CO) values among the investigated ZG GDEs are thus clearly attributed to the dissimilar rate of the CO_2 mass transport due to the different structure of MPLs.

It is important to remind that apart from the abundance of cracks (Figure 2; Figure S2, Supporting Information), the investigated MPLs also differ in void structure and, more specifically, in the porosity in solid regions, as documented by the CR, VR, and PS values (see Table 1). To investigate the effect of cracks and micropores on the observed differences in the catalytic behavior, we plotted FE(CO) values found at the end of the electrolysis as a function of the above three structural parameters in Figure S7, Supporting Information. FE(CO) data plotted on the CR basis shows more evident correlation compared to VR and PS parameters, suggesting that the crack abundance is the most important descriptor of differences in the catalytic behavior. Importantly, results of electrolysis experiments combined with the gas chromatographic product analysis suggest that cracks formed in the MPL prevent (39BB and 39BC) or at least delay (36BB) flooding as an adverse phenomenon frequently reported for $ERCO_2$ employing GDEs.

Apart from FE(CO) values, we also monitored the cell resistance as described in the Experimental Section, and plotted it as a function of time (as well as a function of the passed charge) in Figure 3. For MPLs with high crack abundance (39BB and 39BC), almost constant cell resistance values were found after a short initial period, suggesting that the concentration and mobility distribution of ions in these ZG GDEs reach a steady state. For the ZG GDE with lower crack abundance (36BB), a slight increase in resistance values is detected in later stages of the electrolysis, lagging the decrease of FE(CO) values. The resistance increase is either due to decreased electrolyte conductivity upon the reaction between CO_2 and OH^-[3,9] or a decrease of the active electrode area upon flooding or salt precipitation. Resistance values recorded for the non-cracked ZG GDE (H23C8) show an initial, transient decrease (presumably due to the accumulation of electrolyte ions in the catalyst layer and MPL, vide infra), followed by a pronounced increase

toward the end of the electrolysis. The observed time shifts suggest that the cell resistance monitoring can only detect severe flooding events where the concentration and mobility of ions and/or active area of electrodes are affected significantly. The low flooding predicting power of cell resistance measurements is ascribed to significant resistance contributions originating from the anion exchange membrane and the anolyte, which are not affected by flooding of the GDE. The cell resistance thus cannot be used as an early warning signal to detect the onset of flooding.

Figure 3 further shows electrode potential values, mathematically corrected for the ohmic drop based on the measured cell resistance. Values obtained for ZG GDEs with high abundance of cracks (39BB and 39BC) show only subtle (and uniform) shifts, while more pronounced changes are noticed for the crack-free ZG GDE (H23C8) and the ZG GDE with moderate abundance of cracks (36BB). Such changes are probably due to the transition from the $ERCO_2$ to the ERH_2O regime. Importantly, the onset of changes observed in the electrode potential has no lag to the changes noticed in FE(CO) profiles. This suggests that electrode potential monitoring is applicable as an online tool for the detection of flooding of GDEs at commercially relevant current densities.

In experiments performed with all four ZG GDEs, small amounts of liquids and solids were observed at the back of CFLs, that is, in the gas flow channels and in the outlet equipped with a trap (see Experimental Section for details). After making sure that no electrolyte can escape the electrolyzer via leaking due to loosely assembled parts, we arrived at the conclusion that the observed liquids and solids originate from the transport of the electrolyte through ZG GDEs.

In the literature, the appearance of liquid electrolyte at the back of CFLs (termed as electrolyte perspiration) was attributed to the combination of pressure difference between the electrolyte and the gas phase and the electrowetting phenomena in the interior of GDEs.[37,38] For the ZG GDE electrolyzer employed in our study, the former contribution is given by the difference of the hydrostatic pressure acting on the top of the anion exchange membrane and the pressure in the gas flow channel beneath the CFL (see Figure S1, Supporting Information for the electrolyzer design). The magnitude of the hydrostatic pressure was estimated as 2.5 mbar, being much lower than the value needed to trigger electrolyte perspiration through the 39BC based GDE embedded in a flow-by electrolyzer (15 mbar) reported in the work of DeMot et al.[37]

In our study, the stream of gas (humidified CO_2) was fed to the flow channel at atmospheric pressure. Thus, we conclude that a differential pressure of 2.5 mbar (constant for all four ZG GDEs) was applied to the top of the anion exchange membrane. The pressure exerted on the top of GDE may additionally be influenced by the electroosmotic drag[29] resulting from the electric field (formed due to voltage applied across the cell), acting on the electric double layer in the interior of the membrane. The total pressure applied to the top of GDE is opposed by the capillary pressure originating from its hydrophobic interior structures. It is important to note that the ability of GDEs to resist external pressure may be compromised by electrowetting (an increase of wettability upon applying electric voltage between the electrode and the electrolyte).[30–40]

ADVANCED
SCIENCE NEWS
www.advancedsciencenews.com

small
methods
www.small-methods.com

The magnitude of the capillary pressure is inversely proportional to the characteristic dimensions of interior structures. For hydrophobic surfaces, the electrolyte first enters structures with larger dimensions (cracks in this work), while leaving smaller structures (micropores) dry. For hydrophilic surfaces, the order of the electrolyte intrusion is just the opposite.[81] While wettability is not easily measurable in the interior of GDEs, it may be explored on their surfaces by contact angle measurements. In this work, we have monitored values of the contact angle on the surface of GDEs in the course of their preparation and upon subsequent electrolysis[22,26,27,66,70] performed with systematically varied charge consumption (Figures S8,S9, Supporting Information; see also the Statistical Analysis in the Experimental Section).

All four as-purchased (pristine) GDLs have strongly hydrophobic surfaces, with contact angle values obtained for cracked MPLs ($164° \pm 1°$) being slightly lower than that of the crack-free MPL ($170°$). This is either due to crack walls having higher wettability than solid MPL regions or due to effects of highly curved surfaces. The deposition of the catalyst ink on MPLs leads to the uniform value of $143° \pm 1°$. This is in line with results of above-presented microscopic observations which demonstrate that the catalyst ink permeates to cracks (Figure 2).

Following electrolysis, the measured contact angle values diverge significantly among the employed electrodes. Values obtained for GDEs with high CR values (39BB and 39BC) are time-independent and equal to $106° \pm 2°$, indicating that their surfaces retain hydrophobic character. The value obtained for the GDE with the intermediate CR value (36BB) approaches $90°$, being at the borderline between hydrophobicity and hydrophilicity. For the crack-free GDE (H23C8), contact angle values fall deep in the hydrophilic region. Washing GDEs with deionized water after completing the electrolysis led to uniform contact angle values of $135° \pm 2°$, being slightly lower than that obtained for as-prepared GDEs ($143° \pm 1°$). This partial recovery implies that wettability changes observed upon the electrolysis are largely due to electrolyte accumulated in the GDE and not due to the catalyst degradation. This is in accord with results of identical and random location SEM studies of the catalyst layers presented in Figures S5,S6, Supporting Information.

Besides contact angle measurements, we further monitored the rate of electrolyte perspiration in the course of electrolysis by quantifying the amount of potassium in the outlet trap (Figure 3), employing ICP-MS analysis (see Experimental Section for details). For charge below 510 C cm^{-2}, no potassium was found. For non-cracked ZG GDE, the potassium amount remains low till the end of the electrolysis. For cracked ZG GDEs, amounts are significantly higher, scaling with passed charge and abundance of cracks.

As was already outlined above, the presence of cracks in MPLs helps to retain the catalytic activity of GDEs for a longer time (see the end-electrolysis FE(CO) values correlation with the CR parameter in Figure S7, Supporting Information). This is in agreement with the observation that the surface of GDE cathodes constructed of 39BB and 39BC GDLs show less hydrophobicity loss during electrolysis (Figures S8,S9, Supporting Information), because—as will be demonstrated below—of the cracks of these MPL surfaces act as dominant electrolyte transport pathways. For 36BB, the combination of lower CR

value and hydrophobicity loss leads to slower electrolyte perspiration (Figure 3). Low amounts of potassium found for the non-cracked H23C8 suggest that the capacity of micropores to transport the electrolyte is very limited.

Besides the capillary action originating from interfacial forces, one also needs to consider that the flow of liquids through porous media is affected by viscous forces acting in the liquid. For laminar flow of water through pores of cylindrical geometry, Poiseuille law predicts that the flow rate is proportional to the second power of the cross-sectional pore area. This implies that cracks allow the passage of water at faster rate compared to micropores, additionally supporting the dominant role of cracks in the electrolyte transport. In addition to the presented reasoning, the difference in perspiration rates may further be rationalized by unequal rates of water consumption in the ERCO$_2$ and ERH$_2$O reactions. The two reactions proceed according to

$$CO_2 + H_2O + 2e^- \rightarrow CO + 2OH^- \tag{2}$$

and

$$2H_2O + 2e^- \rightarrow H_2 + 2OH^- \tag{3}$$
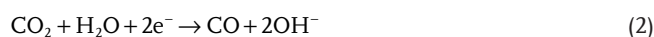
indicating that for ERH$_2$O, the consumption of water per unit passed charge is twice as high as for ERCO$_2$. For the non-cracked ZG GDE, where ERH$_2$O becomes the dominant process soon after the beginning of the electrolysis (Figure 3), higher consumption of water may contribute to the pronounced accumulation of electrolyte ions in the GDE interior, increasing the viscosity and impeding perspiration.

In the following, we further estimate the impact of the electrolyte perspiration on the carbon mass balance in ERCO$_2$, considering the data obtained for ZG GDEs based on 39BB and 39BC as best performing catalytic systems (Figure 3).

As mentioned above, the perspiration results in the accumulation of solids and liquids in gas flow channels and subsequently in the gas outlet equipped with the trap. During the electrolysis, it is not possible to monitor the amount of perspirate in gas flow channels and gas outlet and further analysis is thus restricted to the perspirate found in the trap (see Experimental Section for details). For both ZG GDEs (39BB and 39BC), the amount of potassium found in the trap scales linearly with the consumed charge. For the highest charge (1839 C cm^{-2}), it equals to 6.0 and 7.8 mg, respectively. The electrolyte transported through the GDE is in a permanent contact with gaseous CO$_2$ that is continuously delivered to flow channels. For stoichiometric excess of CO$_2$, we expect that its neutralization proceeds only to the first step, that is, producing HCO$_3^-$ (and not CO$_3^{2-}$). Assuming this stoichiometry, the found mass of potassium corresponds to 1.53 and 1.99×10^{-4} mol of CO$_2$. We further discuss these amounts in the relation to the amount of CO$_2$ electrochemically converted to CO (6.74×10^{-4} mol) obtained considering FE(CO) of 100% for the sake of simplicity. The obtained CO$_2$ loss due to neutralization amounts to 23% and 30% indicating that the electrolyte perspiration cannot be ignored when drawing the total carbon mass balance of ERCO$_2$. Noteworthy, perspiration-related CO$_2$ losses in the ZG GDE electrolyzer as determined in this work

are significantly lower than those reported for CO_2 neutralization in the interior of GDEs embedded in membrane-based flow-by electrolyzers (≈70%).[82,83]

To provide microscopic insight to the electrolyte intrusion in GDEs, we utilized post-experimental SEM imaging to visualize the surfaces and cross sections of electrodes subjected to the electrolysis (see Experimental Section for details). In all inspections, SEM imaging was complemented by EDX mapping of potassium (shown as purple) utilized in this work as the electrolyte cation, to specifically reveal locations to which the electrolyte has permeated. A collection of top-down and cross-sectional SEM images and EDX-K elemental maps are shown in Figure S10, Supporting Information for four different GDE samples and four different electrolysis treatments.

Here, **Figure 4** shows representative top-down EDX maps obtained for surfaces of GDEs subjected to electrolyzes terminated at the charge consumption of 2.8, 170, 510, and 1839 C cm^{-2}. In these surface maps, the deposited salt appears as fuzzy features, sometimes forming islands that, with on-going electrolysis, tend to cover the catalyst layer. Cross-sectional
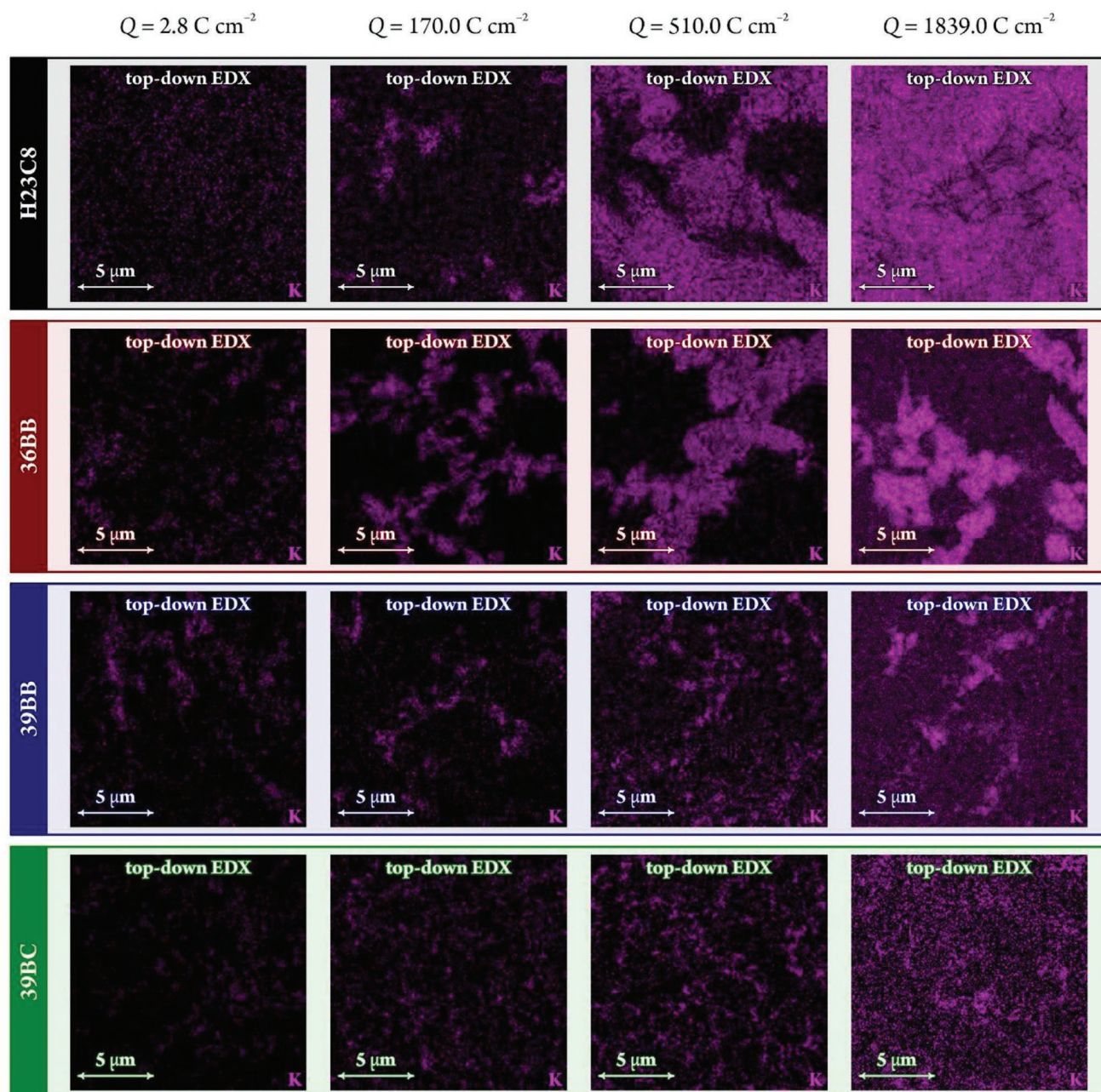

Figure 4. Representative top-down potassium EDX maps obtained for GDEs subjected to electrolyzes performed with varied charge consumption (for a comparison to corresponding top-down SEM images, as well as to cross-sectional SEM images and EDX maps, see Figure S10, Supporting Information).
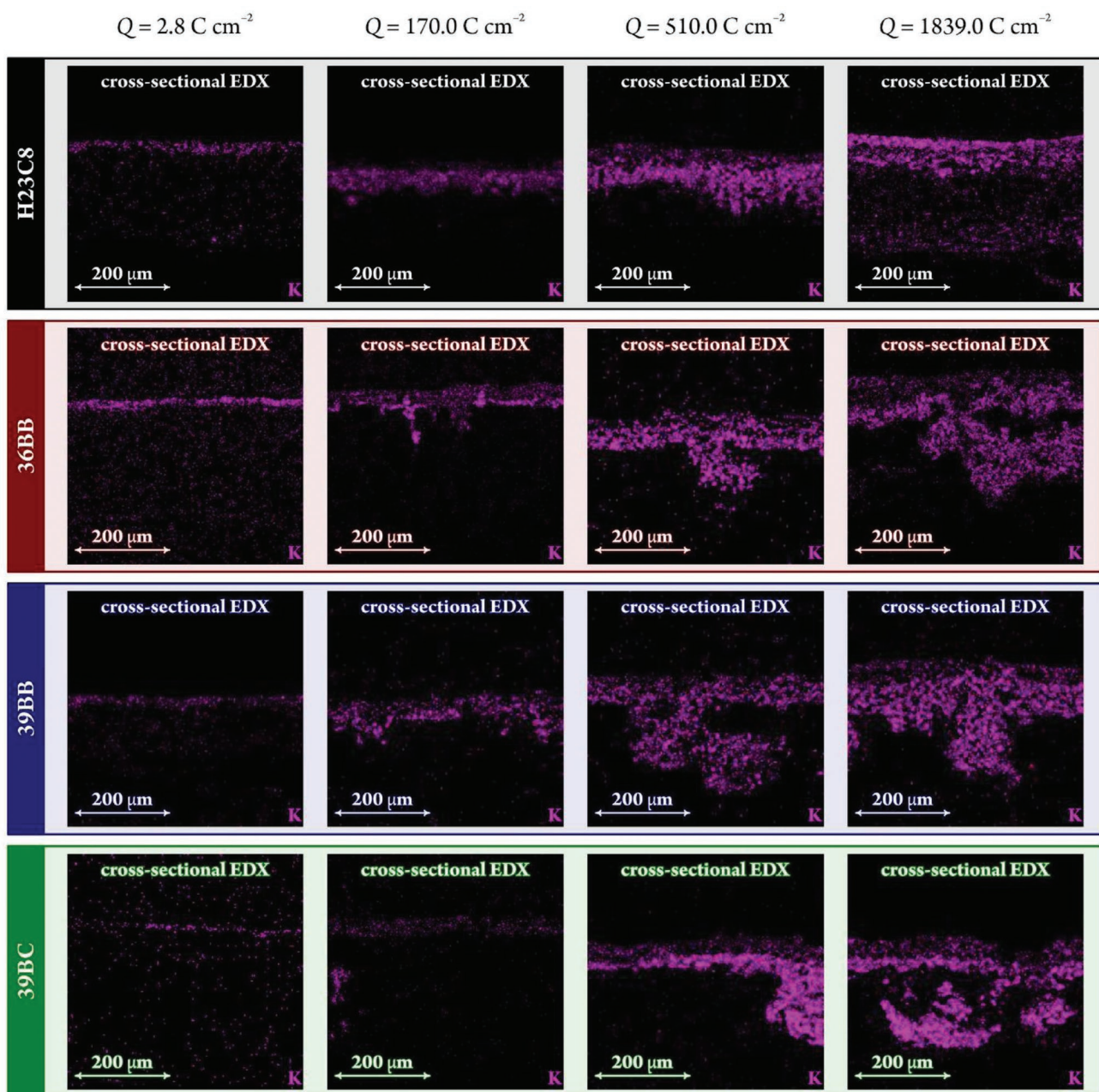
**ADVANCED
SCIENCE NEWS**

www.advancedsciencenews.com

**small
methods**

www.small-methods.com

Figure 5. Representative cross-sectional potassium EDX maps obtained for GDEs subjected to electrolyzes performed with varied charge consumption (for a comparison to corresponding cross-sectional SEM images, as well as to top-down SEM images and EDX maps, see Figure S10, Supporting Information).

K EDX maps, shown in **Figure 5**, confirm that salt deposits (these are assumed to be potassium carbonates or hydrocarbonates), while initially formed only on the surface of the MPL, can later penetrate deeper layers of the GDL structure to different extent. Deposits appear already at the early stage of the electrolysis (2.8 C cm^{-2}) on all four GDE types, however they are confined to the surface of GDEs and show sparse coverage. For later stages of the electrolysis (170, 510, and 1839 C cm^{-2}) the amount and the pattern of deposits markedly differ among electrodes.

For the non-cracked GDE (H23C8), the electrolysis ends up with the deposit completely covering the electrode surface

(Figure 4), being largely confined to the MPL (Figure 5). Only a minor amount of the deposit is found at the bottom of the CFL. This observation is in accordance with the low electrolyte perspiration rate found for this system (Figure 3). For the GDE with the intermediate CR value (36BB), the electrolysis leads to patched deposits covering significant portion of the electrode surface (Figure 4) and more pronounced electrolyte intrusion to the interior of the GDL (Figure 5). Higher amounts of the deposit found at the bottom of the CFL are consistent with higher perspiration rate. For GDEs with high CR values (39BB and 39BC), very little amounts of deposits were found at the

electrode surface (Figure 4), with significant intrusion toward the bottom of the CFL (Figure 5), which is in line with the highest electrolyte perspiration rate.

To reveal relationships between the structure of MPLs and patterns of formed deposits, we further performed SEM imaging at higher magnification, together with combined EDX mapping of silver and potassium, with representative results shown in Figure S11, Supporting Information. All inspections were performed on GDEs subjected to electrolyzes terminated after 510 C cm^{-2}. The non-cracked GDE (H23C8) shows that the silver signal is confined to the top of the MPL and the potassium signal is evenly distributed mainly in the MPL, with little intrusion toward the CFL, all being in accord with the above-presented results (Figures 2,4,5). The SEM image obtained for 36BB shows a crack in the middle, with a corresponding region of increased silver signal. The potassium signal is localized mostly beneath this crack. A very similar scenario is observed for 39BB, with the crack, silver signal and potassium signal being in the left part of the inspected region. For 39BC, the SEM image depicts a horizontal rupture in the MPL in the central part of the micrograph with corresponding increase of the silver signal and the potassium signal located mostly below the rupture.

To conclude, high-resolution cross-sectional imaging of GDEs combined with EDX mapping of silver and potassium as signatures of cracks and electrolyte intrusion clearly demonstrate that these features correlate. This unique approach thus provides microscopic evidence that cracks drain excess electrolyte from the MPL, which is macroscopically observed in the form of electrolyte perspiration.

Samples of electrodes subjected to electrolyzes terminated at varied stages were further analyzed by ICP-MS with the goal of determining the total amount of potassium in their interior (see Experimental Section for details). Results are shown as potassium mass normalized to the electrode area (numbers stated in mg cm^{-2} shown in the panels of **Figure 6**). It is worth noting that the ICP-MS technique, while it can provide the absolute amount of potassium in the entire volume of the GDE,[74] lacks information about its spatial distribution. On the contrary, cross-sectional EDX mapping of potassium gives access to the spatial distribution,[34,35,68,69,72,76] but provides no information in terms of the absolute concentration. The two techniques may be combined to provide spatially resolved absolute potassium profiling as demonstrated by our recent contribution.

Following the approach described before,[77] we quantified the potassium distribution in GDEs subjected to electrolysis with the charge consumption varied as described above. Obtained local absolute potassium concentration values were averaged along horizontal lines of EDX maps and plotted as a function of the vertical position (i.e., depth in the GDE), with results depicted as shaded profiles in Figure 6. To provide statistically relevant information, such obtained profiles were further averaged over five individually prepared GDE cross sections, with results shown as thick curves. The concentration scale is established based on the ICP-MS based measurement of the total (surface area normalized) K content of the studied GDE section, providing the integral of the thick curves in Figure 6.

The MPL regions are visualized by shaded bands in Figure 6. The thickness of CFLs as imaged upon the electrolysis was generally found to differ a little from that determined for as-purchased GDLs (see Table 1). We attribute these differences to the swelling of the CFL structure due to electrolyte intrusion.

At early stages of electrolysis (charge consumption of 2.8 C cm^{-2}), little amounts of potassium were observed inside the investigated GDEs (Figure 6), being confined to the top of MPLs. At 170 C cm^{-2}, potassium permeated deeper to the GDE structure, with more pronounced accumulation noticed for systems losing their catalytic activity (H23C8 and 36BB, Figure 3) in top regions of the MPL. Differences among GDEs are most marked at later stages of the electrolysis (510 and 1839 C cm^{-2}). For H23C8, potassium stays localized mostly in the MPL and the top part of the CFL, with very little intrusion found in its bottom part, which is in line with the low perspiration rate observed for this GDE (Figure 3). For 36BB, the intrusion advances deeper to the CFL, being consistent with higher perspiration rate. Among all four GDEs, 36BB shows the highest total potassium content in the GDE presumably due to the combination of highly porous MPL (Table 1), high wettability of the catalyst layer (Figures S8,S9, Supporting Information) and low abundance of cracks as draining features (Table 1, Figure 2; Figure S2, Supporting Information). For 39BB and 39BC, overall lower concentration values in both MPL and CFL are observed, being in accord with the highest perspiration rates and the highest abundance of cracks.

For all four ZG GDEs, the total amount of potassium (numbers in mg cm^{-2} in Figure 6) grows up to 510 C cm^{-2} and converges to a plateau for 1839 C cm^{-2}, suggesting that a steady-state electrolyte intrusion is approached. No distinct correlations were found between the total amount of potassium in GDEs after completing the electrolysis at 1839 C cm^{-2} and the void parameters of MPLs (Figure S7, Supporting Information) suggesting that both cracks and micropores play a role in the accumulation of potassium in MPLs. The highest amount of potassium observed for 36BB presumably reflects a relatively high porosity of its MPL (Table 1) and high wettability of the catalyst layer (Figures S8,S9, Supporting Information), both favoring electrolyte intrusion, combined with low abundance of cracks (Figure 2; Figure S2, Supporting Information) impeding electrolyte perspiration.

For the three cracked GDEs (36BB, 39BB, and 39BC), the amount of potassium found in their interior (Figure 6) is insignificant compared to that determined in the outlet trap (Figure 3). This finding corroborates that cracks function as efficient pathways for the electrolyte transport and indicates that the total amount of CO_2 deposited as carbonates in the interior of GDEs can be neglected in the total carbon balance of $ERCO_2$.

We further inspected the back sides of GDEs subjected to the electrolysis by SEM/EDX analysis, finding only little amounts of potassium (Figure S12, Supporting Information). Contact angle measurements performed after the electrolysis with 1839 C cm^{-2} also confirmed that back sides of GDEs largely retained their hydrophobic character (Figure S13, Supporting Information).

To explore the extent of the electrolyte flooding in the absence of CO_2, we further carried out an electrolytic experiment employing argon-fed 36BB based ZG GDE selected for the demonstration. The catalytic activity of such treated
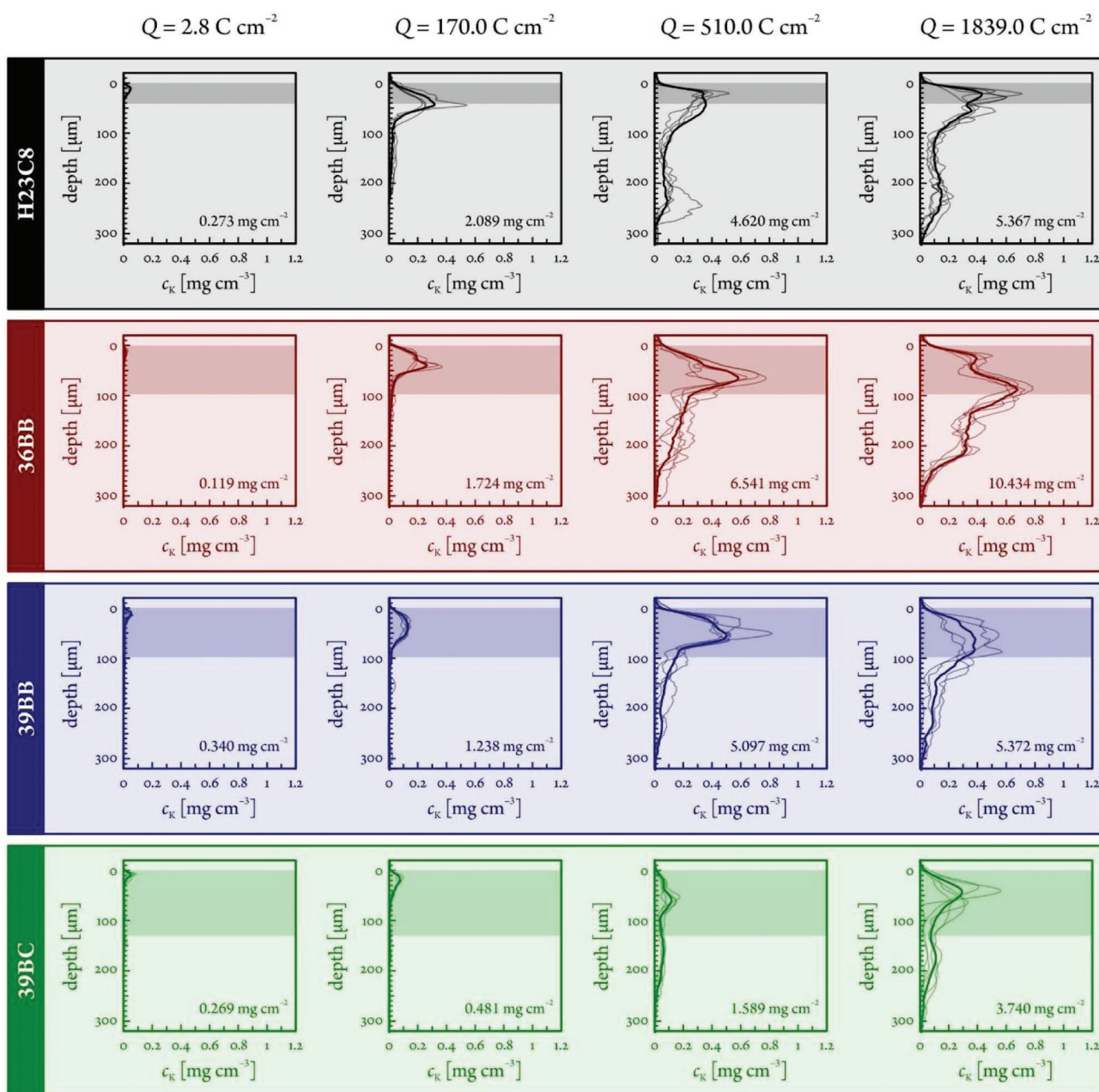
ADVANCED
SCIENCE NEWS
www.advancedsciencenews.com

small
methods
www.small-methods.com

Figure 6. Potassium concentration as a function of depth in cross sections of GDEs subjected to electrolysis performed with varied charge consumption, obtained by combined EDX/ICP-MS approach. Shaded bands indicate MPL regions. The total amount of potassium found in the GDE by ICP-MS, normalized to its surface area, is indicated by numbers. See the Statistical Analysis in the Experimental Section for more information on data processing.

electrode was subsequently inspected in a follow-up electrolysis performed with CO_2. Resulting FE(CO) values (Figure S14, Supporting Information, left panel) were significantly lower compared to those obtained for the as-prepared GDE (Figure 3). This indicates that flooding in the GDE takes place also in the absence of CO_2 and in situ generated (hydrogen)carbonate salts. Nonetheless, when a cleaning/drying step (see the Experimental Section for details) was inserted between the argon-fed and the follow-up CO_2-fed electrolysis, the evolution of the catalytic activity (Figure S14, Supporting Information, right panel)

well resembled that obtained for the as-prepared GDE. This demonstrates that flooded electrolyte may be removed from the interior of GDE when flooding has taken place in the absence of CO_2.

Results of the multi-methodological experimental approach presented above have revealed significant differences in the evolution of catalytic activity and the character of the electrolyte intrusion among inspected ZG GDEs due to varied structure of their MPLs. In the following, we aim to find relationships between the MPL structure, electrolyte intrusion pattern, and
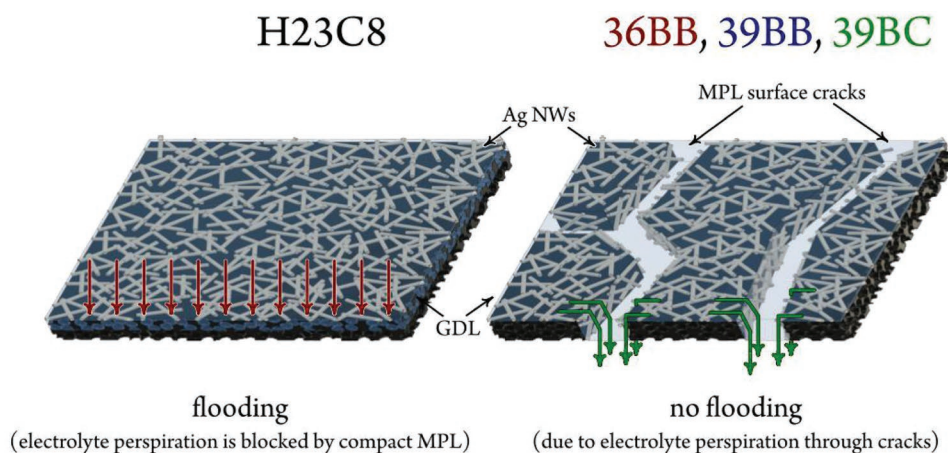
**ADVANCED
SCIENCE NEWS**

www.advancedsciencenews.com

**small
methods**

www.small-methods.com

Figure 7. Schematic depiction of the catalyst layer supported with non-cracked (left) and cracked (right) MPL, visualizing electrode flooding and electrolyte perspiration phenomena.

catalytic activity, and provide mechanistic insights in these phenomena, employing a schematic depiction of the catalyst layers supported by non-cracked and cracked MPLs shown in **Figure 7**.

The MPL of H23C8 contains no cracks (Figure 2; Figure S2, Supporting Information) and shows low internal porosity (Table 1). The electrolysis performed with such ZG GDE leads to an immediate and pronounced decline in FE(CO), significant increase in cell resistance and voltage (Figure 3), loss of hydrophobilicy (Figures S8,S9, Supporting Information) and electrode surface completely covered with potassium (Figure 4) that additionally accumulates in the MPL and top part of CFL (Figures 4,5). All these characteristics are indicative of severe flooding of the MPL (Figure 7, left), with the proposed mechanism presented as follows. The combination of the hydrostatic pressure and electroosmotic drag drives the electrolyte through the anion exchange membrane to the catalyst layer, where water is partially consumed in cathodic processes (first $ERCO_2$, later mainly ERH_2O). In the absence of cracks in the MPL, the excess electrolyte floods its micropores.[81] The presence of the liquid electrolyte in micropores significantly reduces the diffusion coefficient of CO_2.[5] The diffusion rate slows down in the course of the electrolysis as the electrolyte intrudes deeper in the GDL (Figures 4,5). The ERH_2O takes place in the GDL,[70] causing more water to be consumed per unit charge. This accelerates the accumulation of OH^- ions (both originally present in the electrolyte and generated as the by-product of ERH_2O) in the GDL. Increased amounts of OH^- ions are balanced by potassium ions that reach the GDL by ionic migration via the anion exchange membrane that can generally have non-perfect permselectivity.[84] Increased ionic concentration may negatively impact the solubility of gases[85] and reaction kinetics.[3,86] The absence of cracks combined with low internal porosity of the MPL and increased electrolyte viscosity due to accumulated ions leads to low perspiration rate (Figure 3). Furthermore, OH^- ions react with CO_2 dissolved in the electrolyte to form (hydrogen)carbonate anions, reducing the electrolyte conductivity and increasing the risk of the salt precipitation in micropores. The accumulation of ions further leads to loss of hydrophobicity facilitating flooding of micropores.[68]

Based on the results of consecutive electrolytic experiments performed with argon and CO_2 (Figure S14, Supporting Information), we support the view that flooding is not initiated by the carbonate precipitation, being in contradiction to the interpretation presented by Leonard et al.[68] In fact, the intrusion of the electrolyte to micropores may be triggered by electrowetting at extreme cathodic potentials (Figure 3).[30–40] It is important to note that the ex situ SEM/EDX analysis of GDE cross sections, as performed in this work (Figures 4,5), can visualize areas to which the electrolyte has permeated during the electrolysis but cannot distinguish whether solid precipitates are formed during or after the electrolysis.[69]

The MPL of 36BB contains cracks in low abundance (Figure 2; Figure S2, Supporting Information) and has high internal porosity (Table 1). Compared to the crack-free system, this ZG GDE sustains $ERCO_2$ for longer time, shows lower increase in the cell resistance and voltage (Figure 3), less pronounced loss of hydrophobicity (Figures S8,S9, Supporting Information) and lower accumulation of potassium on the electrode surface (Figures 4,5). Compared to micropores, cracks have much greater characteristic dimensions (Figure 2; Figure S2, Supporting Information) and thus constitute preferred pathways for the electrolyte intrusion (Figure 7, right), which was microscopically confirmed by the SEM/EDX analysis (Figure S11, Supporting Information) and macroscopically observed as increased perspiration rate (Figure 3). The perspiration through cracks alleviates the flooding of micropores, enabling them to function as channels for the gas transport.[53,54,56–58] However, the loss of catalytic activity (Figure 3) accompanied by a significant buildup of potassium on the surface (Figure 4) and in the interior (Figure 5) of the GDE observed in later stages of the electrolysis indicate that the crack abundance in 36BB is not sufficient to maintain micropores dry. Values of contact angles found in later stages of the electrolysis are close to 90° (Figures S8,S9, Supporting Information), suggesting that capillary forces have minimal effect on the electrolyte transport through the MPL. In such case, the electrolyte transport rate via cracks and micropores is governed by their hydrodynamic resistance.

MPLs of 39BB and 39BC have high abundance of cracks (Figure 2; Figure S2, Supporting Information) and high

internal porosity (Table 1). They differ in the architecture of cracks, with 39BB having higher amount of narrow cracks and 39BC having broader cracks with sparser abundance. Both ZG GDEs show near-unity FE(CO) values, no increase in the cell resistance, only subtle cell voltage shifts, high electrolyte perspiration rates (Figure 3), almost no loss of hydrophobicity (Figures S8,S9, Supporting Information) and little accumulation of potassium on the electrode surface (Figure 4) and in its interior (Figures 4,5), with all these characteristics being retained for the entire time span of the electrolysis. This indicates that MPLs of these two electrodes possess sufficient abundance of cracks enabling efficient electrolyte perspiration that prevents the flooding of micropores (Figure 7, right). A desired electrolyte management in the ZG GDE, with the liquid phase being largely confined to the catalyst layer, is thus established.[4] Slightly higher FE(CO) values obtained for the 39BC based system further corroborate that cracks, and not micropores, are the main drainage pathway for the electrolyte perspiration, providing valuable hints for the design of MPLs in future ERCO$_2$ electrolyzers. Near unity FE(CO) values combined with results of cross-sectional EDX mapping of silver indicate that Ag nanowires deposited on crack walls are catalytically active toward ERCO$_2$. In fact, the catalyst located in the interior of cracks may be more active than that deposited on the MPL surface due to facilitated CO$_2$ transport, as recently demonstrated by Welch et al.[78] Nevertheless, it is important to note that the electrolyte perspiration through cracks causes parasitic CO$_2$ losses due to neutralization occurring in gas flow channels, which needs to be accounted for when assessing the overall economic viability of newly designed electrolyzers.

3. Conclusions and Outlook

Cracks as structures naturally occurring in MPLs of GDEs have been reported as beneficial for the water removal in polymer electrolyte membrane fuel cells.

In this work, we have inspected the ability of cracks to improve the electrolyte management and the overall catalytic performance of zero gap GDEs for the electrochemical reduction of carbon dioxide. The employed electrodes contained silver nanowires in a thin catalytic layer and differed in the abundance of cracks in the MPL supporting the catalyst. Utilizing galvanostatic electrolyzes, we demonstrated that electrodes with appropriate abundance of cracks show high and sustained catalytic activity, while a fast transition to parasitic reduction of water was noticed for non-cracked electrodes.

Small amounts of liquids and solids were observed in flow channels and the outlet of the carbon dioxide delivery system indicating that the electrolyte is transported through zero gap GDEs (electrolyte perspiration). For the first time, the amount of the electrolyte in the perspirate was determined, employing ICP-MS, finding that this amount scales with the abundance of cracks.

Cross sections of GDEs subjected to electrolyzes were subsequently inspected by our recently developed analytical approach combining SEM imaging, EDX elemental analysis, and ICP-MS, to obtain absolute concentration profiles of potassium used as the electrolyte intrusion marker. The performed analysis provided the microscopic evidence that cracks serve as preferential pathways for the electrolyte transport through the MPL. Cracks thus drain excess electrolyte from the catalytic layer, which prevents flooding of micropores and enables them to function as efficient transport channels for gaseous carbon dioxide. In the absence of cracks, the electrolyte was found to flood micropores, reflecting itself as greatly reduced catalytic activity.

Our contribution presents the first study focusing on the effect of cracks on the electrolyte management and catalytic activity in the field of electrochemical CO$_2$ reduction. Besides monitoring the electrolyte intrusion in GDEs as a function of charge consumed in the electrolysis, we found correlations among the catalytic performance, electrochemical characteristics of cells, electrolyte perspiration rates, and surface wettability of electrodes, resolving the influence of cracks and micropores in the electrolyte transport.

While cracks were clearly proven to be beneficial for the electrolyte management, it should not be forgotten that the electrolyte perspiration occurring via these structures leads to non-negligible parasitic losses of carbon dioxide due to its neutralization. Therefore, efforts to optimize the utilization of carbon dioxide in electrolyzers must include searching for conditions under which both electrode flooding and perspiration-related reactant losses are minimized. Following the approaches reported for polymer electrolyte membrane fuel cells, we further aim at manufacturing and inspecting zero gap GDEs based on MPLs modified with artificially created draining elements such as holes or trenches formed by mechanical or laser perforation. The electrolyte perspiration through these structures may be controlled by their dimensions and predicted employing numerical models taking into account the capillary action, hydrodynamic resistance, and electroosmotic drag.

4. Experimental Section

Preparation of Gas Diffusion Electrodes: All experiments performed in this work employed commercial GDLs composed of supporting compressed CFL (carbon without additives) and MPL (carbon black treated with 5% PTFE). MPLs differ in their height, porosity, and abundance of cracks (for details see Results and Discussion). The GDL with crack-free MPL (H23C8) was obtained from Freudenberg, while GDLs involving cracked MPLs (36BB, 39BB, and 39BC) were purchased from Sigracet.

Silver nanowires used in this work as catalysts for ERCO$_2$ were synthesized following the procedure described in the previous work.[87] To prepare the catalyst ink, 4.5 mg of the as-synthesized Ag nanowires and 0.8 mg of carbon black (VULCAN VXC72R, Cabot) were separately dispersed in 20 mL of isopropanol (BASF SE, assay ≥ 99.0%) and sonicated for 30 min. Such prepared dispersions were intermixed, sonicated for 30 min, and dried by a rotary evaporator (Büchi R 210, 40 °C, 65 mbar). The resulting mixture was re-dispersed in 18 mL of isopropanol additionally containing 180 µL of Nafion 117 solution (≈5 wt% in a mixture of lower aliphatic alcohols and water, obtained from Sigma Aldrich) and sonicated for 20 min. The thus prepared catalyst ink was deposited on the MPL surfaces by airbrushing (hand-held Airbrushpistole Infinity CR plus, propelled by nitrogen gas, 99.999%, Carbagas, Switzerland), forming the catalyst layer. Such modified assemblies were dried and used as GDEs in electrolytic experiments performed as follows.

Assembly of the Electrolyzer: All electrochemical experiments performed in this work were realized in the electrolyzer shown in Figure S1,

Supporting Information.[22,79] The electrolyzer was based on ZG GDE arrangement with GDEs prepared as described above, interfaced to the anodic compartment. The assembly of the electrolyzer was carried out as follows. The GDE with the catalyst layer facing upward was placed on a stainless steel support functioning as a current collector and a gas delivery system (it was equipped with flow channels connected to inlet and outlet tubing). The anion exchange membrane (X37-50 RT, Dioxide materials) was subjected to a pre-treatment suggested by the supplier, and gently placed on the top of the GDE. The formed ZG GDE was covered by a Teflon chamber, which was subsequently mounted to the stainless steel support by a clamp. The Teflon chamber was filled with aqueous KOH solution (10 mL, 2 M, pH = 14.3, solid KOH purchased from Sigma Aldrich, prepared employing Milli-Q water) serving as the anolyte. The Teflon chamber contained a central circular orifice (radius of 0.15 cm) in its bottom part defining the geometrical area of the ZG GDE/anolyte interface. Iridium wire (99.9%, MaTeck Material-Technologie & Kristalle GmbH, Germany) separated by glass frit and Ag/AgCl/3 M KCl electrode (double junction design, Metrohm) were immersed in the anolyte and were utilized as the counter electrode and the reference electrode. A flask containing 15 mL of Milli-Q water was placed downstream to the gas outlet and served as a trap to collect the perspirate resulting from the electrolyte transport through the ZG GDE.

Electrochemical Measurements: The catalytic activity of the ZG GDE (set as the working electrode) was inspected by galvanostatic experiments in the electrolyzer assembled as described above, employing an ECi-200 potentiostat (ECi-200, Nordic Electrochemistry). For all four GDEs, the electrolysis was performed at current of −20 mA (corresponding to geometric current density of −283 mA cm^{-2}) for systematically varied time, specifically 10, 600, 1800, and 6500 s. In the Results and Discussion section, the duration of electrolysis is presented as passed charge normalized to the geometrical area of the ZG GDE/anolyte interface (0.0707 cm^2). Unless otherwise specified, a freshly prepared GDE was used in the electrolysis. A humidified gaseous CO$_2$ stream (99.999%, Carbagas, Switzerland) was continuously supplied to the flow channels of the stainless steel support via the inlet at the rate of 18 mL min^{-1} employing a thermal mass flow controller (red-y smart, Vögtlin Instruments). The gaseous mixture leaving the outlet was fed through a drying tube and its composition was analyzed for CO and H$_2$ by online GC (SRI Instruments) in 10 min intervals.[21] The formed CO and H$_2$ quantities, measured during electrolysis, added up to about 100% ± 10% of the quantities that could be expected from the charge of electrolysis. Noting that while the formation of some other products (e.g., that of formate) was possible in very little amount in the studied electrolyzer, it was assumed that the H$_2$:CO ratios detectable by GC were, within range of experimental error, correct. Faradaic efficiency values (e.g., those presented in Figure 3) were thus re-scaled so that the measured H$_2$:CO ratios were respected, together accounting for a 100% Faradaic efficiency.

The cell voltage and resistance were monitored in 0.1 s intervals. The cell resistance was obtained by superimposing AC perturbation (5 000 Hz, 50 µA) to the current applied to the cell (20 mA) and monitoring the AC component of the cell voltage.

For the GDE based on 36BB GDL, a follow-up electrolysis experiment was performed with the goal of exploring the possibility of restoring the catalytic activity of once used electrode. First, the GDE was subjected to the electrolysis performed as described above. Afterward, the electrolyzer was disassembled and the GDE was immersed in ≈30 mL of quiescent Milli-Q water for 5 min, the procedure being repeated 7 times. Subsequently, the GDE was dried in a vacuum oven for 2 h at ambient temperature. Such treated GDE was reinstalled into the electrolyzer and its catalytic performance was inspected in a follow-up electrolysis carried out under the same conditions.

Also for the GDE based on 36BB GDL, an additional control electrolytic experiment was performed to inspect the occurrence of flooding in the absence of CO$_2$. First, the GDE was subjected to the electrolysis with humidified CO$_2$ being replaced by humidified argon (99.9999%, Carbagas, Switzerland). Subsequently, the electrolyzer was disassembled and the GDE was either subjected to the cleaning/drying

procedure performed as described above or this step was omitted. Such treated GDE was reinstalled into the electrolyzer and its catalytic performance was inspected in a follow-up electrolysis carried out with humidified CO$_2$.

Characterization of Electrodes: Surfaces of pristine MPLs and as-prepared GDEs were inspected by optical microscopic imaging employing a VHX600 Keyence digital microscopes. The obtained images were utilized to determine the surface CR based on counting pixels corresponding to cracks and solid regions on the MPL surface. The void ratio of CFLs, MPLs, and entire GDLs was obtained by using a pycnometer, employing isopropanol as a liquid that was assumed to completely fill up the internal structures of layers. Surfaces of as-purchased (pristine) MPLs, as-prepared GDEs, and GDEs subjected to the electrolysis were additionally inspected by white light interferometry (Contour GT, Bruker) equipped with Vision64 software (Vision64, Bruker).

A Zeiss Gemini 450 SEM equipped with an EDX spectroscopy instrument (Aztec, Oxford instruments) was used to investigate the structure and content of silver and potassium on surfaces and in the interior of GDEs. Surfaces of GDEs were inspected before and after electrolytic measurements performed as described above. For selected samples, identical location SEM studies were performed. Subsequently, electrodes subjected to the electrolysis were frozen in liquid nitrogen and cut by a sharp blade and such obtained cross sections were examined by SEM/EDX. To obtain statistically significant information, at least five cross sections were prepared and analyzed for each GDE. The cross-sectional imaging was additionally performed for as-purchased GDLs, to determine the thickness of the CFL and the MPL.

The mass loading of silver in the catalyst layer of as-prepared GDEs was determined by means of ICP-MS (NexION 2000 ICP-MS instrument, PerkinElmer). For this purpose, GDEs of circular shape with the radius of 0.1 cm were prepared and examined. GDE samples were introduced to concentrated nitric acid (69.3%, VLSI selectipur, BASF), sonicated for 30 min and left overnight. Additionally, ICP-MS analysis following the same sample treatment was employed to determine the amount of potassium in the interior of GDEs upon the electrolysis. Furthermore, the ICP-MS was employed to determine the amount of potassium in the perspirate resulting from the electrolyte transport through GDEs, found in the trap following the gas outlet.

The wettability of as-purchased GDLs, as prepared GDEs and GDEs subjected to electrolysis performed as described above was assessed by contact angle measurement (Krüss Advance Drop Shape Analyzer DSA25, Krüss GmbH, Hamburg, Germany). Electrodes subjected to the electrolysis were dried for 2 h before actual measurements. All inspected samples were mounted on a flat stage, sessile water drops (Milli-Q water, 1.4 µL) were deposited on their top at room temperature and contact angles were recorded immediately after creating droplets.

Statistical Analysis: For data presented in the form expected value ± error in the paper, the expected value was determined as the arithmetic mean, and the error as the standard deviation of the dataset. Contact angle intervals reported in the text were calculated using values shown in Figure S7, Supporting Information, by averaging over different GDEs that underwent the same electrolysis treatment. The optical micrographs of the as-prepared GDEs (Figure 2) were used for the calculation of surface CRs of the GDEs. The micrographs were utilized to determine the surface CR based on counting pixels corresponding to cracks and solid regions on the MPL surface: the analysis was done by an in-house developed algorithm written in LabVIEW. The void ratios of the carbon fibrous and MPLs of GDLs, as well as the total void ratios of CFLs, MPLs, and entire GDLs, shown in Table 1, were determined by three parallel pycnometer-based densitometry measurements. The vertical depth profiles of K$^+$ concentrations, shown in Figure 6, were created using cross-sectional EDX maps obtained from the respective GDEs following electrolyzes. The total (average) K$^+$ concentrations, corresponding to the integrals of the averaged distribution curves, were determined by a single ICP-MS measurement. In case of each panel of Figure 6, several (five to eight) individual EDX maps were analyzed. These maps were obtained in a numerical format from the Aztec controlling software. Depth profiles were

**ADVANCED
SCIENCE NEWS**

www.advancedsciencenews.com

**small
methods**

www.small-methods.com

obtained by a row-to-row summation of the K signal intensity, followed by vertical alignment of the individual distributions. This alignment was based on the assignation of a 0 depth value to the first entry where the detected K intensity reached 3 times the initial noise level. For the alignment, subsequent averaging, and normalization of the distributions, a home-built software (written in LabVIEW) was used; more details of the calculations can be found elsewhere.[77] Raw data serving as a basis for the presented calculations are accessible at Zenodo.[88]

Supporting Information

Supporting Information is available from the Wiley Online Library or from the author.

Acknowledgements

Conflict of Interest

The authors declare no conflict of interest.

Data Availability Statement

The raw data to this paper are made fully accessible to the public via Zenodo (https://doi.org/10.5281/zenodo.6421142) along with the publication of this manuscript.

Keywords

[1] I. Ganesh, *Renewable Sustainable Energy Rev.* **2016**, *59*, 1269.
[2] S. Nitopi, E. Bertheussen, S. B. Scott, X. Y. Liu, A. K. Engstfeld, S. Horch, B. Seger, I. E. L. Stephens, K. Chan, C. Hahn, J. K. Norskov, T. F. Jaramillo, I. Chorkendorff, *Chem. Rev.* **2019**, *119*, 7610.
[3] T. Burdyny, W. A. Smith, *Energy Environ. Sci.* **2019**, *12*, 1442.
[4] N. T. Nesbitt, T. Burdyny, H. Simonson, D. Salvatore, D. Bohra, R. Kas, W. A. Smith, *ACS Catal.* **2020**, *10*, 14093.
[5] D. M. Weekes, D. A. Salvatore, A. Reyes, A. X. Huang, C. P. Berlinguette, *Acc. Chem. Res.* **2018**, *51*, 910.
[6] E. W. Lees, B. A. W. Mowbray, F. G. L. Parlane, C. P. Berlinguette, *Nat. Rev. Mater.* **2022**, *7*, 55.
[7] A. Z. Weber, J. Newman, *J. Electrochem. Soc.* **2005**, *152*, A677.
[8] B. Kim, F. Hillman, M. Ariyoshi, S. Fujikawa, P. J. A. Kenis, *J. Power Sources* **2016**, *312*, 192.
[9] E. J. Dufek, T. E. Lister, M. E. McIlwain, *Electrochem. Solid-State Lett.* **2012**, *15*, B48.
[10] S. S. Bhargava, F. Proietto, D. Azmoodeh, E. R. Cofell, D. A. Henckel, S. Verma, C. J. Brooks, A. A. Gewirth, P. J. A. Kenis, *ChemElectroChem* **2020**, *7*, 2001.
[11] S. Verma, Y. Hamasaki, C. Kim, W. X. Huang, S. Lu, H. R. M. Jhong, A. A. Gewirth, T. Fujigaya, N. Nakashima, P. J. A. Kenis, *ACS Energy Lett.* **2018**, *3*, 193.
[12] S. Verma, X. Lu, S. C. Ma, R. I. Masel, P. J. A. Kenis, *Phys. Chem. Chem. Phys.* **2016**, *18*, 7075.
[13] B. Kim, S. Ma, H. R. M. Jhong, P. J. A. Kenis, *Electrochim. Acta* **2015**, *166*, 271.
[14] C. M. Gabardo, A. Seifitokaldani, J. P. Edwards, C. T. Dinh, T. Burdyny, M. G. Kibria, C. P. O'Brien, E. H. Sargent, D. Sinton, *Energy Environ. Sci.* **2018**, *11*, 2531.
[15] V. R. Stamenkovic, D. Strmcnik, P. P. Lopes, N. M. Markovic, *Nat. Mater.* **2017**, *16*, 57.
[16] J. Lee, J. Lim, C. W. Roh, H. S. Whang, H. Lee, *J. CO₂ Util.* **2019**, *31*, 244.
[17] L. C. Weng, A. T. Bell, A. Z. Weber, *Energy Environ. Sci.* **2019**, *12*, 1950.
[18] A. Angulo, P. van der Linde, H. Gardeniers, M. Modestino, D. F. Rivas, *Joule* **2020**, *4*, 555.
[19] L. Cindrella, A. M. Kannan, J. F. Lin, K. Saminathan, Y. Ho, C. W. Lin, J. Wertz, *J. Power Sources* **2009**, *194*, 146.
[20] M. L. Liu, Y. Kong, H. F. Hu, N. Kovacs, C. Z. Sun, I. Z. Montiel, M. D. G. Vazquez, Y. Hou, M. Mirolo, I. Martens, J. Drnec, S. Vesztergom, P. Broekmann, *J. Catal.* **2021**, *404*, 371.
[21] M. D. Galvez-Vazquez, S. Alinejad, H. F. Hu, Y. H. Hou, P. Moreno-Garcia, A. Zana, G. K. H. Wiberg, P. Broekmann, M. Arenz, *Chimia* **2019**, *73*, 922.
[22] M. D. Galvez-Vazquez, P. Moreno-Garcia, H. Xu, Y. H. Hou, H. F. Hu, I. Z. Montiel, A. V. Rudnev, S. Alinejad, V. Grozovski, B. J. Wiley, M. Arenz, P. Broekmann, *ACS Catal.* **2020**, *10*, 13096.
[23] M. Maja, C. Orecchia, M. Strano, P. Tosco, M. Vanni, *Electrochim. Acta* **2000**, *46*, 423.
[24] N. Wagner, M. Schulze, E. Gulzow, *J. Power Sources* **2004**, *127*, 264.
[25] Z. Xing, X. Hu, X. F. Feng, *ACS Energy Lett.* **2021**, *6*, 1694.
[26] Z. Xing, L. Hu, D. S. Ripatti, X. Hu, X. F. Feng, *Nat. Commun.* **2021**, *12*, 136.
[27] W. H. Lee, Y. J. Ko, Y. Choi, S. Y. Lee, C. H. Choi, Y. J. Hwang, B. K. Min, P. Strasser, H. S. Oh, *Nano Energy* **2020**, *76*, 105030.
[28] U. O. Nwabara, A. D. Hernandez, D. A. Henckel, X. Y. Chen, E. R. Cofell, M. P. De-Heer, S. Verma, A. A. Gewirth, P. J. A. Kenis, *ACS Appl. Energy Mater.* **2021**, *4*, 5175.
[29] A. Reyes, R. P. Jansonius, B. A. W. Mowbray, Y. Cao, D. G. Wheeler, J. Chau, D. J. Dvorak, C. P. Berlinguette, *ACS Energy Lett.* **2020**, *5*, 1612.
[30] T. Burchardt, *J. Power Sources* **2004**, *135*, 192.
[31] K. Liu, W. A. Smith, T. Burdyny, *ACS Energy Lett.* **2019**, *4*, 639.
[32] A. Lowe, C. Rieg, T. Hierlemann, N. Salas, D. Kopljar, N. Wagner, E. Klemm, *ChemElectroChem* **2019**, *6*, 4497.
[33] K. J. Puring, D. Siegmund, J. Timm, F. Mollenbruck, S. Schemme, R. Marschall, U. P. Apfel, *Adv. Sustainable Syst.* **2021**, *5*, 2000088.
[34] F. Bienen, A. Lowe, J. Hildebrand, S. Hertle, D. Schonvogel, D. Kopljar, N. Wagner, E. Klemm, K. A. Friedrich, *J. Energy Chem.* **2021**, *62*, 367.
[35] F. Bienen, J. Hildebrand, D. Kopljar, N. Wagner, E. Klemm, K. A. Friedrich, *Chem. Ing. Tech.* **2021**, *93*, 1015.
[36] K. L. Yang, R. Kas, W. A. Smith, T. Burdyny, *ACS Energy Lett.* **2021**, *6*, 33.
[37] B. De Mot, J. Hereijgers, M. Duarte, T. Breugelmans, *Chem. Eng. J.* **2019**, *378*, 122224.
[38] P. Jeanty, C. Scherer, E. Magori, K. Wiesner-Fleischer, O. Hinrichsen, M. Fleischer, *J. CO₂ Util.* **2018**, *24*, 454.
[39] M. Duarte, B. De Mot, J. Hereijgers, T. Breugelmans, *ChemElectroChem* **2019**, *6*, 5596.
[40] S. Sen, S. M. Brown, M. Leonard, F. R. Brushett, *J. Appl. Electrochem.* **2019**, *49*, 917.

[41] D. G. Wheeler, B. A. W. Mowbray, A. Reyes, F. Habibzadeh, J. F. He, C. P. Berlinguette, *Energy Environ. Sci.* **2020**, *13*, 5126.

[42] B. Endrodi, E. Kecsenovity, A. Samu, F. Darvas, R. V. Jones, V. Torok, A. Danyi, C. Janaky, *ACS Energy Lett.* **2019**, *4*, 1770.

[43] M. E. Leonard, M. J. Orella, N. Aiello, Y. Roman-Leshkov, A. Forner-Cuenca, F. R. Brushett, *J. Electrochem. Soc.* **2020**, *167*, 124521.

[44] H. Li, Y. H. Tang, Z. W. Wang, Z. Shi, S. H. Wu, D. T. Song, J. L. Zhang, K. Fatih, J. J. Zhang, H. J. Wang, Z. S. Liu, R. Abouatallah, A. Mazza, *J. Power Sources* **2008**, *178*, 103.

[45] K. Jiao, X. G. Li, *Prog. Energy Combust. Sci.* **2011**, *37*, 221.

[46] N. Yousfi-Steiner, P. Mocoteguy, D. Candusso, D. Hissel, A. Hernandez, A. Aslanides, *J. Power Sources* **2008**, *183*, 260.

[47] P. C. Pei, H. C. Chen, *Appl. Energy* **2014**, *125*, 60.

[48] M. B. Ji, Z. D. Wei, *Energies* **2009**, *2*, 1057.

[49] A. Bazylak, *Int. J. Hydrogen Energy* **2009**, *34*, 3845.

[50] S. Tsushima, S. Hirai, *Prog. Energy Combust. Sci.* **2011**, *37*, 204.

[51] R. Omrani, B. Shabani, *Int. J. Hydrogen Energy* **2017**, *42*, 28515.

[52] S. Tsushima, S. Hirai, *J. Therm. Sci. Technol.* **2015**, *10*, JTST0002.

[53] T. Sasabe, P. Deevanhxay, S. Tsushima, S. Hirai, *Electrochem. Commun.* **2011**, *13*, 638.

[54] E. A. Wargo, V. P. Schulz, A. Cecen, S. R. Kalidindi, E. C. Kumbur, *Electrochim. Acta* **2013**, *87*, 201.

[55] M. P. Manahan, S. Kim, E. C. Kumbur, M. M. Mench, *ECS Trans.* **2009**, *25*, 1745.

[56] H. Markotter, I. Manke, P. Kruger, T. Arlt, J. Haussmann, M. Klages, H. Riesemeier, C. Hartnig, J. Scholta, J. Banhart, *Electrochem. Commun.* **2011**, *13*, 1001.

[57] N. Karst, V. Faucheux, A. Martinent, P. Bouillon, J. P. Simonato, *J. Power Sources* **2010**, *195*, 5228.

[58] J. S. Ma, X. X. Zhang, Z. Y. Jiang, H. Ostadi, K. Jiang, R. Chen, *Fuel* **2014**, *136*, 307.

[59] D. Gerteisen, C. Sadeler, *J. Power Sources* **2010**, *195*, 5252.

[60] K. Nishida, T. Murakami, S. Tsushima, S. Hirai, *J. Power Sources* **2010**, *195*, 3365.

[61] R. L. Cook, R. C. Macduff, A. F. Sammells, *J. Electrochem. Soc.* **1990**, *137*, 607.

[62] G. L. De Gregorio, T. Burdyny, A. Loiudice, P. Iyengar, W. A. Smith, R. Buonsanti, *ACS Catal.* **2020**, *10*, 4854.

[63] M. Jouny, W. Luc, F. Jiao, *Nat. Catal.* **2018**, *1*, 748.

[64] J. J. Lv, M. Jouny, W. Luc, W. L. Zhu, J. J. Zhu, F. Jiao, *Adv. Mater.* **2018**, *30*, 1803111.

[65] C. M. Gabardo, C. P. O'Brien, J. P. Edwards, C. McCallum, Y. Xu, C. T. Dinh, J. Li, E. H. Sargent, D. Sinton, *Joule* **2019**, *3*, 2777.

[66] E. R. Cofell, U. O. Nwabara, S. S. Bhargava, D. E. Henckel, P. J. A. Kenis, *ACS Appl. Mater. Interfaces* **2021**, *13*, 15132.

[67] C. T. Dinh, T. Burdyny, M. G. Kibria, A. Seifitokaldani, C. M. Gabardo, F. P. G. de Arquer, A. Kiani, J. P. Edwards, P. De Luna, O. S. Bushuyev, C. Q. Zou, R. Quintero-Bermudez, Y. J. Pang, D. Sinton, E. H. Sargent, *Science* **2018**, *360*, 783.

[68] M. E. Leonard, L. E. Clarke, A. Forner-Cuenca, S. M. Brown, F. R. Brushett, *ChemSusChem* **2020**, *13*, 400.

[69] D. McLaughlin, M. Bierling, R. Moroni, C. Vogl, G. Schmid, S. Thiele, *Adv. Energy Mater.* **2020**, *10*, 2000488.

[70] D. Raciti, T. Braun, B. M. Tackett, H. Xu, M. Cruz, B. J. Wiley, T. P. Moffat, *ACS Catal.* **2021**, *11*, 11945.

[71] G. O. Larrazabal, P. Strom-Hansen, J. P. Heli, K. Zeiter, K. T. Therldldsen, I. Chorkendorff, B. Seger, *ACS Appl. Mater. Interfaces* **2019**, *11*, 41281.

[72] J. Li, G. X. Chen, Y. Y. Zhu, Z. Liang, A. Pei, C. L. Wu, H. X. Wang, H. R. Lee, K. Liu, S. Chu, Y. Cui, *Nat. Catal.* **2018**, *1*, 592.

[73] A. Patru, T. Binninger, B. Pribyl, T. J. Schmidt, *J. Electrochem. Soc.* **2019**, *166*, F34.

[74] B. De Mot, M. Ramdin, J. Hereijgers, T. J. H. Vlugt, T. Breugelmans, *ChemElectroChem* **2020**, *7*, 3839.

[75] B. Endrodi, E. Kecsenovity, A. Samu, T. Halmagyi, S. Rojas-Carbonell, L. Wang, Y. Yan, C. Janaky, *Energy Environ. Sci.* **2020**, *13*, 4098.

[76] B. Endrodi, A. Samu, E. Kecsenovity, T. Halmagyi, D. Sebok, C. Janaky, *Nat. Energy* **2021**, *6*, 439.

[77] Y. Kong, H. F. Hu, M. L. Liu, Y. Hou, V. Kolivoska, S. Vesztergom, P. Broekmann, *J. Catal.* **2022**, *408*, 1.

[78] A. J. Welch, A. Q. Fenwick, A. Bohme, H. Y. Chen, I. Sullivan, X. Q. Li, J. S. DuChene, C. X. Xiang, H. A. Atwater, *J. Phys. Chem. C* **2021**, *125*, 20896.

[79] G. K. H. Wiberg, M. Fleige, M. Arenz, *Rev. Sci. Instrum.* **2015**, *86*, 024102.

[80] Y. H. Hou, N. Kovacs, H. Xu, C. Z. Sun, R. Erni, M. D. Galvez-Vazquez, A. Rieder, H. F. Hu, Y. Kong, M. L. Liu, B. J. Wiley, S. Vesztergom, P. Broekmann, *J. Catal.* **2021**, *394*, 58.

[81] L. C. Weng, A. T. Bell, A. Z. Weber, *Phys. Chem. Chem. Phys.* **2018**, *20*, 16973.

[82] M. Ma, S. Kim, I. Chorkendorff, B. Seger, *Chem. Sci.* **2020**, *11*, 8854.

[83] M. Ma, E. L. Clark, K. T. Therkildsen, S. Dalsgaard, I. Chorkendorff, B. Seger, *Energy Environ. Sci.* **2020**, *13*, 977.

[84] G. M. Geise, M. A. Hickner, B. E. Logan, *ACS Appl. Mater. Interfaces* **2013**, *5*, 10294.

[85] M. Roehe, A. Botz, D. Franzen, F. Kubannek, B. Ellendorff, D. Oehl, W. Schuhmann, T. Turek, U. Krewer, *ChemElectroChem* **2019**, *6*, 5671.

[86] N. T. Nesbitt, W. A. Smith, *J. Phys. Chem. C* **2021**, *125*, 13085.

[87] H. F. Hu, M. L. Liu, Y. Kong, N. Mysuru, C. Z. Sun, M. D. Galvez-Vazquez, U. Muller, R. Erni, V. Grozovski, Y. H. Hou, P. Broekmann, *ACS Catal.* **2020**, *10*, 8503.

[88] Y. Kong, M. Liu, H. Hu, Y. Hou, S. Vesztergom, M. de J. Gálvez-Vázquez, I. Zelocualtecatl Montiel, V. Kolivoška, P. Broekmann, Raw data for the article "Cracks as efficient tools to mitigate flooding in gas diffusion electrodes used for the electrochemical reduction of carbon dioxide" **2022**, https://doi.org/10.5281/zenodo.6421142.